



# In Situ Investigations of Simultaneous Two-Layer Slot Die Coating of Component-Graded Anodes for Improved High-Energy Li-Ion Batteries

Ralf Diehm,\* Jana Kumberg, Christopher Dörrer, Marcus Müller, Werner Bauer, Philip Scharfer, and Wilhelm Schabel

The use of thicker electrodes can contribute to a reduction in cell costs. However, the properties of the electrode must be kept in view to be able to meet the performance requirements. Herein, the possibility of simultaneous multilayer slot die coating is investigated to improve the electrode properties of medium- and high-capacity anodes. The stable coating window of the two-layer slot die coating process is investigated to produce property-graded multilayer electrodes. Electrodes with different styrene-butadiene rubber (SBR) gradients are investigated with regard to adhesive force and electrochemical performance. An increase in the adhesive force of up to 43.5% and an increase in the discharge capacity is observed.

## 1. Introduction

Since the first commercialization of lithium-ion batteries (LIBs) in 1991, the range of applications has expanded considerably. In the beginning of this technology, the battery cells were used especially for consumer electronics and power tools. The development of this battery technology gave battery-powered devices an enormous boost.<sup>[1]</sup> In recent years, the mobility sector has become the focus of attention, especially with the growing markets of electric vehicles (EVs), hybrid electric vehicles (HEVs), and plug-in hybrid electric vehicles (PHEVs). This process is driven by rapidly falling battery costs and the need for locally

R. Diehm, J. Kumberg, C. Dörrer, Dr. P. Scharfer, Prof. W. Schabel  
Institute of Thermal Process Engineering (TVT), Thin Film Technology (TFT)  
Karlsruhe Institute for Technology (KIT)  
Kaiserstr. 12, 76131 Karlsruhe, Germany  
E-mail: ralf.diehm@kit.edu

Dr. M. Müller, Dr. W. Bauer  
Institute of Applied Materials – Energy Storage Systems (ESS)  
Karlsruhe Institute for Technology (KIT)  
Hermann-von-Helmholtz-Platz 1, 76144 Eggenstein-Leopoldshafen,  
Germany

The ORCID identification number(s) for the author(s) of this article can be found under <https://doi.org/10.1002/ente.201901251>.

© 2020 The Authors. Published by WILEY-VCH Verlag GmbH & Co. KGaA, Weinheim. This is an open access article under the terms of the Creative Commons Attribution License, which permits use, distribution and reproduction in any medium, provided the original work is properly cited.

DOI: 10.1002/ente.201901251

emission-free vehicles.<sup>[2]</sup> Studies show a need of more than 1 TWh of production capacity by 2025, which represents a significant increase in production capacity.<sup>[3]</sup>

In addition, further cost reduction and improvement of the electrode properties are also necessary. One concept is to reduce costs by manufacturing thick electrodes. Due to the higher electrode capacity, the number of electrodes and associated inactive materials such as collector foils and separators in the battery cell are saved. The energy density is also increased by saving inactive materials. Previous investigations have shown that thick electrodes lose capacities especially at higher charging

and discharging rates.<sup>[4]</sup> The production of two-layer coatings with a graded electrode might lower this problem. Simultaneous multilayer coating is a cost-efficient way of manufacturing films with stacked layers of different compositions to adjust the layer properties. This can be used to counteract known problems such as binder migration during drying, which reduces the adhesion to the current collector.<sup>[5–11]</sup> The use of more binders to improve the adhesion force, however, reduces the discharge capacity of the cell. The stability of simultaneous two-layer slot die coating was fundamentally investigated in different works.<sup>[12,13]</sup> For cathode coatings, the influence of the simultaneous application of two layers with binder gradient and carbon black gradient was investigated, and improvements to the electrode properties were found.<sup>[14,15]</sup> So far, multilayer coating is not yet widely used for commercial electrodes. It has not yet been clarified whether multilayer coating also has an advantage for anodes and, in particular, how the coating stability behaves in comparison with the individual layers previously used.

## 2. Results and Discussions

The aim of this work is to investigate the stability of simultaneous two-layer Li-ion anode coatings with a two-layer slot die. Therefore, a new experimental setup was designed. A detailed description can be found in the Experimental Section. The manufactured electrodes are examined with regard to their properties to show the advantages of the simultaneous two-layer coating process. The anode slurry was prepared in one batch with carboxymethyl cellulose (CMC) binder but without styrene-butadiene rubber (SBR) binder. The SBR binder was then mixed

into individual batches. Multilayer electrodes with different binder gradients were produced and evaluated with regard to adhesive strength and electrochemical performance.

## 2.1. Layer Configuration and Slurry Properties

For the investigation, a gradient of SBR binder was applied during the simultaneous two-layer coating by combining two slurries with different SBR contents. All electrodes consist of a bottom layer with 50% layer thickness at the current collector and a top layer with 50% layer thickness near the separator. In this work, three simultaneous two-layer configurations (A + A, B1 + B2, and C1 + C2) were produced with different binder gradients. For reference, single-layer electrodes were produced with the respective slurry on the current collector (A only, B1 only, and C1 only). A schematic cross section of the produced anodes is shown in **Figure 1**. The composition of the slurries used in this study is shown in **Table 1**.

Starting with the same composition in reference configuration A, the binder gradient is increased with configuration B1 + B2 to two-thirds at the current collector and one-third at the separator to a maximum gradient in configuration C1 + C2, where the entire SBR binder is in the bottom layer.

The viscosity of the slurries was examined in a plate–plate rheometer with shear rates from 0.01 to 5000 s<sup>-1</sup>. The slurries show a strong shear thinning behavior with 129 ± 10 Pa s at 0.01 s<sup>-1</sup> for all slurries and from 0.16 Pa s (P4) to 0.26 Pa s (P0) at 5000 s<sup>-1</sup> (**Figure 2**). The viscosity decreases with higher addition of the SBR binder. This is due to the dilution of the slurries by water contained in the SBR binder dispersion and may be enhanced by the addition of dispersant obtained in the latex binder for stabilizing the dispersion. All slurries used in this

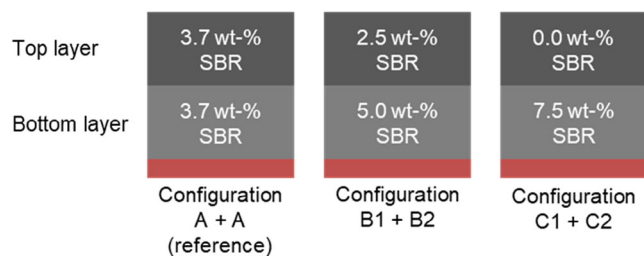


**Figure 1.** Schematic cross section of the multilayer stacks. Numbers indicate the different contents of SBR binder in wt%. Configuration A + A is the reference electrode with the same amount of SBR binder in top and bottom layers. Configuration B1 + B2 is two-thirds of the SBR binder in the bottom and only one-third in the top layer. In C1 + C2, the SBR binder is only in the bottom layer during coating.

**Table 1.** Overview of the slurry composition.

ID	Graphite [wt%]	CB [wt%]	CMC [wt%]	SBR [wt%]	Solids [wt%]
C2	96.60	1.45	1.95	0	43.9
B2	94.20	1.42	1.89	2.49	43.3
A	93.00	1.40	1.87	3.73	43.0
B1	91.80	1.38	1.85	4.97	42.7
C1	89.40	1.34	1.80	7.46	42.2

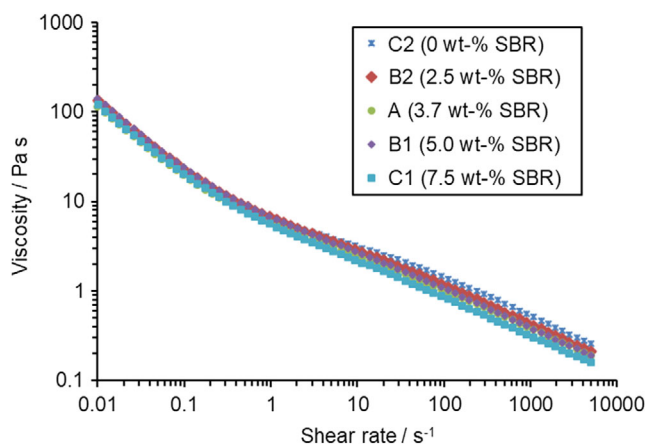


**Figure 2.** Average viscosity of the different anode slurries as a function of the applied shear rate. All slurries show a very strong shear thinning behavior. With addition of SBR binder, the solid content is reduced, and thus the viscosity is reduced.

work show a gel-like behavior and differ in their behavior from slurries with liquid behavior due to the very high zero shear viscosity. The surface tension of the slurries is 0.066 Nm<sup>-1</sup>.

Electrodes with the different configurations A + A, B1 + B2, and C1 + C2 were produced for two area weights, first, with a normal capacity of about 2.05 mAh g<sup>-1</sup> and second, with a high capacity of about 7.96 mAh g<sup>-1</sup>. **Table 2** shows an overview on the thicknesses and weights of the tested electrodes.

## 2.2. Coating Stability

The coating stability of simultaneous two-layer slot die coating was investigated with the configuration A + A, i.e., the same SBR binder content in both layers. Two different coating gaps of 127 μm for medium-capacity electrodes and 420 μm for very-high-capacity electrodes were used. The fraction of the wet film thickness is 50% in the upper layer and 50% in the lower layer with the same viscosity in both slurries. The coatings were examined for three failure criteria: 1) air entrainment, where air is introduced into the film through the moving contact line, 2) swelling, in which the slurry is moving against the web direction outside the coating bead, and 3) layer intermixing, where the film is intermixed inside the coating bead. In addition, the

**Table 2.** Overview of electrodes: wet film thickness, dry film thickness, and area weight.

Electrode configuration	Capacity	Wet film thickness (adjusted) [μm]	Dry film thickness (noncalendered) [μm]	Area weight [g m <sup>-2</sup> ]	Area capacity (theo.) [mAh cm <sup>-2</sup> ]
A + A	Medium	116	65.8 ± 1.1	59.9 ± 1.3	2.0
B1 + B2	Medium	116	66.2 ± 0.5	59.1 ± 1.3	2.0
C1 + C2	Medium	116	69.3 ± 0.1	64.1 ± 0.4	2.1
A + A	High	426	223.3 ± 1.1	237.0 ± 0.8	7.9
B1 + B2	High	426	228.6 ± 6.5	238.7 ± 6.7	8.0
C1 + C2	High	426	227.2 ± 2.4	233.7 ± 3.3	7.8

stability behavior was simulated based on studies by Schmitt et al.<sup>[16]</sup> Although a copper foil is used as a substrate for all experiments regarding dry anode coatings, the experimental setup requires a transparent polyethylene terephthalate (PET) substrate to visualize the coating failure mechanism in the wet film.

**Figure 3** shows views of the coating bead (bottom view) and the corresponding views on top of the coated film (top view) for stable coating, air entrainment coating defect, and swelling coating defect. The bottom layer is highlighted by ultraviolet (UV) tracer and glows blue under UV light, the top layer without UV tracer is black.

Figure 3 shows the view from below through the PET film onto the slot die outlet to the coating bead. The coating bead with the moving contact line of a defect-free coating is shown in Figure 3, II. The corresponding top view in Figure 3, III shows no coating defects. However, if the volume flow is too low (Figure 3, IV), the moving contact line is not stable and air inclusions are introduced into the film. These are expressed as bubbles or streaks in the film (Figure 3). In contrast, if the

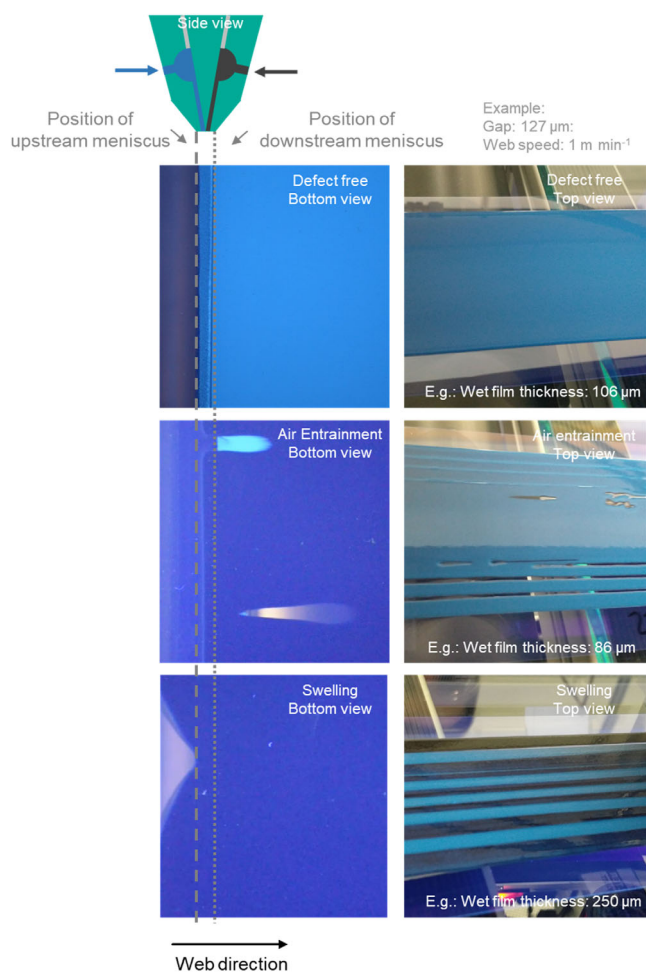


**Figure 3.** Examples of bottom view and top view at different coating conditions. Exit of the two slots of the slot die in bead mode (I). Defect-free coating (II and III), air entrainment (IV and V), and swelling (VI and VII). Dotted lines mark the edges of the slot die lips. Blue glowing UV marker illuminates the lower layer through the PET film.

volume flow is too high (Figure 3, VI), the liquid is pressed out of the coating bead against the coating direction. This results in mixed stripes in the coating (Figure 3, VII). For investigation of the coating stability, the images for every coating condition with different coating speeds and wet film thicknesses were evaluated and divided into three categories, defect free, lower limit, and upper limit. The region between defect-free coating and coating with defects is termed coating window.

The coating stability for the lower gap of 127  $\mu\text{m}$  is shown in **Figure 4**. At 0.5  $\text{m min}^{-1}$ , the minimum wet film thickness at which no air entrainment could be observed is 87  $\mu\text{m}$ . This minimum wet film thickness increases slightly to 90  $\mu\text{m}$  at 20  $\text{m min}^{-1}$  with a peak at 1  $\text{m min}^{-1}$ . The maximum wet film thickness before swelling could be observed which starts at 147  $\mu\text{m}$  at 0.5  $\text{m min}^{-1}$  and decreases to 133  $\mu\text{m}$  at 20  $\text{m min}^{-1}$ . In the stable coating area between the stability limits, wet film thickness can be varied without coating defects. No layer intermixing occurs between these stability limits.

In addition to the experimental data, simulated limits based on the calculated pressure distribution in the coating bead according to Schmitt et al. are shown in **Figure 5** and 6.<sup>[16]</sup> For the state-of-the-art electrode with a gap width of 127  $\mu\text{m}$ , the limit is well predicted by simulation. The maximum possible wet film

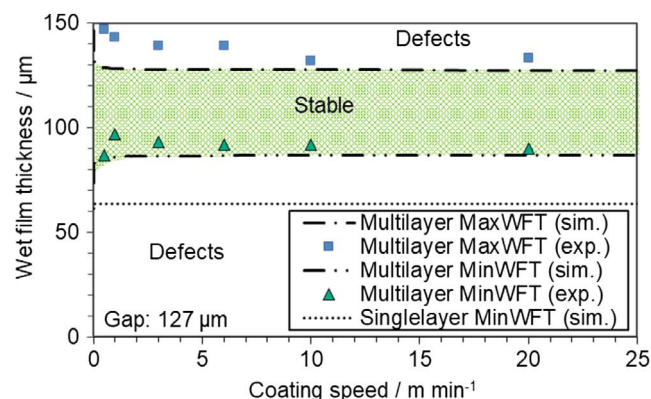


**Figure 4.** Coating window for the simultaneous two-layer coating of anode slurry with a coating gap of 127  $\mu\text{m}$  (state-of-the-art thickness). The stability behavior was also simulated according to Schmitt et al.<sup>[16]</sup>

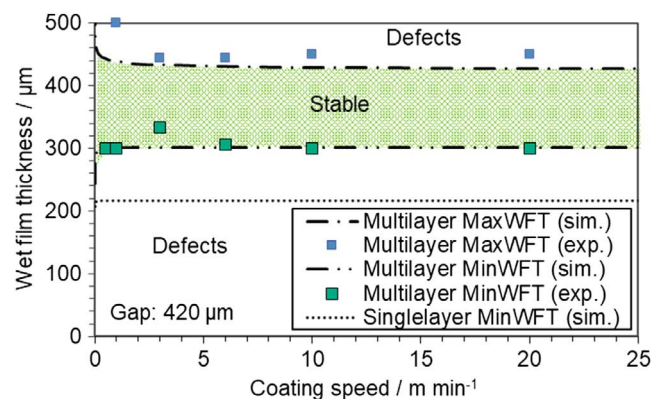


**Figure 5.** Coating window for the simultaneous two-layer coating of anode slurry with a coating gap of 420  $\mu\text{m}$  (high-energy cells).

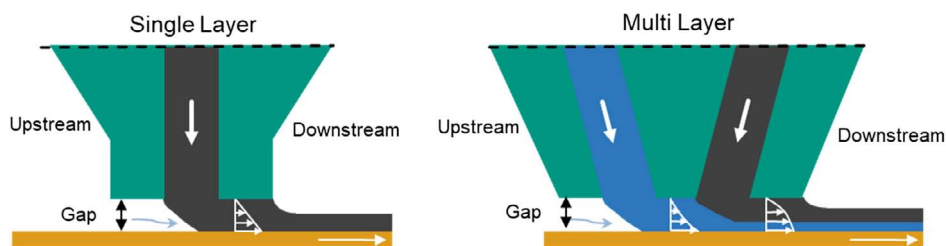


**Figure 6.** Schematic flow profile at the limit to the minimum wet film thickness for single layers (left) and multilayers (right).

thickness is slightly above the gap width at a higher web speed. For the minimum wet film thickness, the experimental values are slightly higher than the simulation at low speeds of  $1 \text{ m min}^{-1}$ . At higher speeds, the simulation and experimental values fit together very well. The minimum wet film thickness for multilayers is considerably higher than the minimum for the single layers. In this case  $64 \mu\text{m}$  for the single layer and  $90 \mu\text{m}$  for the multi-multilayer at  $20 \text{ m min}^{-1}$ . For the larger gap of  $420 \mu\text{m}$ , the coating stability window is shown in Figure 5.

The lower limit at the larger gap of  $420 \mu\text{m}$  is constant at  $300 \mu\text{m}$  wet film thickness, with an outlier at  $3 \text{ m min}^{-1}$  with  $333 \mu\text{m}$ . The higher limit increases from  $510 \mu\text{m}$  at  $0.5 \text{ m min}^{-1}$  to  $450 \mu\text{m}$  at  $20 \text{ m min}^{-1}$ . The comparison of experimental and simulated limits shows an agreement of the simulation. The minimum wet film thickness for multiple layers is significantly higher than for single layers as well. This is caused by the flow conditions at the upstream meniscus. The pressure balance for the simulation is approximately balanced if a Couette flow forms in the gap without superimposition of a Poiseuille flow. This is the case when the wet film thickness is half of the gap of the single-layer coating. For multilayer coatings, the lower layer, which in this investigation corresponds to 50% of the wet film thickness, is decisive. In the case of multilayers, this flow differs from the one in a single-layer slot die, because two volume flows result due to the two feeding slots of the multilayer slot die. For a stable coating with minimal wet film thickness, Couette and Poiseuille flows are superimposed for multilayers, resulting in higher wet film thicknesses. Schematic drawings of the flow profile are shown in Figure 6 for single-layer and multilayer coatings.

In addition to the presented failure criteria of air entrainment and swelling, there is also the coating defect of intermixing of both layers. With the presented experimental setup and the UV-active marking of one layer intermixing was visualized, as shown in Figure 7.

The intermixing of the two layers, with the bottom layer colored blue with UV tracer and the black top layer without coloring, can be detected optically. Process points where intermixing occurred are shown in Figure 8.

The experimentally determined process points with mixing are below the simulation of the minimum wet film thickness specified by air entrainment. Thus the failure criteria of intermixing could only be observed at very low coating speeds of  $0.2$  and  $0.5 \text{ m min}^{-1}$ . No intermixing was detected at coating speeds higher than  $1 \text{ m min}^{-1}$  and above the minimum wet film thickness.

As shown in the literature, intermixing is caused by backflows within the coating beads and the resulting forced

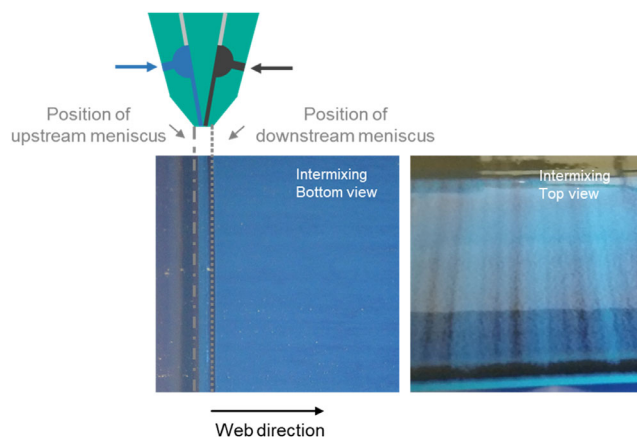


**Figure 7.** Examples of top and bottom views with intermixing of both layers. Gap  $h_G = 127 \mu\text{m}$ . Web speed  $u_{\text{web}} = 0.2 \text{ m min}^{-1}$ . Wet film thickness  $h_{\text{wft}} = 69 \mu\text{m}$  (50% top layer and 50% bottom layer).

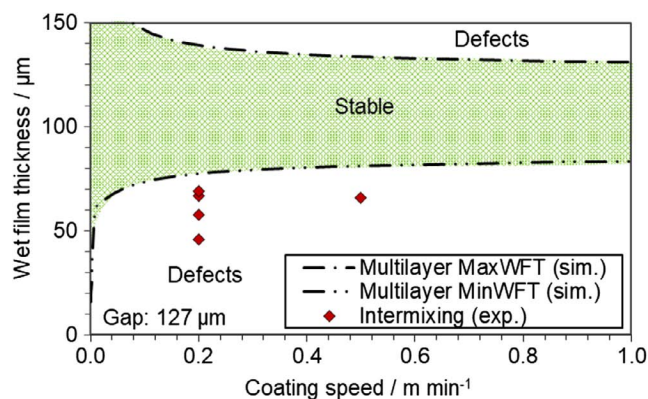


**Figure 8.** Coating window with observed process points of intermixing of both layers. The simulated process limits for the minimum wet film thickness MinWFT and the maximum wet film thickness MaxWFT are shown.

vortices.<sup>[12]</sup> Nam and Carvalho show that this occurs at layer thicknesses of the bottom layer less than one-third of the gap distance. For the battery coatings used in this study, coating thickness ratios of 50% in the bottom and 50% in the top layer were investigated. This ratio leads to a critical bottom layer thickness well below the minimum wet film thickness in the relevant speed range and therefore outside the process window.

In summary, the two-layer coating of anode slurries is possible with a sufficiently large stability range between lower and upper limits and without film intermixing.

### 2.3. Adhesive Force

The adhesive force represents a measuring method which can give a benchmark for binder migration.<sup>[7]</sup> It has already been shown in previous studies that the drying rate has a high influence on the adhesive force.<sup>[5,7,17]</sup> For this reason, the drying rate was kept constant at  $1.5 \text{ g m}^{-2} \text{ s}^{-1}$  in this article. **Figure 9** shows the adhesive force of the active material on the copper substrate of the different-layer configurations. For comparison, single layers were also produced with the binder concentration corresponding to the lower layer.

The adhesive force is mainly determined by the SBR content in the position close to the collector foil. The greater this proportion, the higher the adhesive force. By doubling the SBR directly on the current collector, the adhesive force also increases to approximately twice this amount (from  $23 \text{ N m}^{-1}$  with 3.7 wt% SBR to  $44 \text{ N m}^{-1}$  with 7.4 wt% SBR in single layers). This is evident both for the single layers and for the multilayer configurations. The adhesive force with single layers with uniform binder distribution during coating is just as high as that of a double layer. With the double layer, however, only the lower layer to the current collector has the same binder content as the single layer, whereas the upper layer has considerably less binder. The increase in adhesive force is 26.5% for the mean binder gradient B1 + B2 ( $29.1 \text{ N m}^{-1}$  compared with  $23 \text{ N m}^{-1}$  of the reference) and 43.5% for the maximum binder gradient C1 + C2 ( $43.5 \text{ N m}^{-1}$  compared with  $23 \text{ N m}^{-1}$  of the reference). Multilayer electrodes with SBR binder gradient can therefore lead to a significant reduction in the total binder content without any negative impact on adhesion. There is no significant influence of the layer thickness on the adhesive force observed

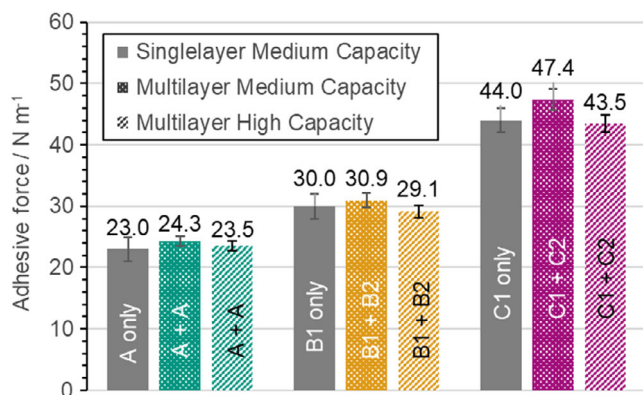


**Figure 9.** Adhesive force between active material layer and copper foil for the different layer configurations: Single-layer and multilayer medium capacity ( $2.05 \pm 0.08 \text{ mAh cm}^{-2}$ ) and multilayer high capacity ( $7.96 \pm 0.16 \text{ mAh cm}^{-2}$ ). For comparison, single-layer electrodes were produced with the slurry corresponding to the lower layer and medium-capacity thickness. The single layer shows a similar adhesive force as the multilayer configurations, but the multilayers contain fewer SBR binders in total (Table 1). The adhesive force increases with more SBR binder contents in the current collector layer.

for these electrodes. Thicker electrodes with high capacities show only a slightly lower adhesive force with 3% (A + A), 6% (B1 + B2), and 8% (C1 + C2), compared with medium-capacity electrodes. This differs significantly from experience in literature,<sup>[17]</sup> where a decreasing adhesive force with a higher layer thickness is observed. This may be due to different fluid structures with a high zero shear viscosity in this work compared with the literature. As described in the Experimental Section, a high intensive kneading step was used for mixing, which leads to a gel-like paste structure. While in the literature, a dissolver was used as a mixing device which leads to a different rheological behavior.

### 2.4. Electrochemical/cell Test

The specific discharge capacity is important for assessing the quality of the different electrode configurations. As no suitable cathode was available for the  $7.96 \text{ mAh cm}^{-2}$  anode, only cells with the capacity of  $2.05 \text{ mAh cm}^{-2}$  were characterized in full cells. The influence of the layer configurations on the specific discharge capacity of full cells with normal capacity is shown in **Figure 10**.

For charging, only a constant current (CC) step was used. The average capacity of the different-layer configurations is approximately the same at very low C rates of C/20 ( $145.5 \pm 1.6 \text{ mAh g}^{-1}$  for A + A,  $143.8 \pm 1.2 \text{ mAh g}^{-1}$  for B1 + B2, and  $143.0 \pm 1.2 \text{ mAh g}^{-1}$  for C1 + C2). With increasing the C rate to 2C, the specific discharge capacity increases from  $102.2 \pm 1.1 \text{ mAh g}^{-1}$  (A + A, reference) to  $105.2 \pm 1.9 \text{ mAh g}^{-1}$  (B1 + B2, +2.9%) and  $107.2 \pm 0.9 \text{ mAh g}^{-1}$  (C1 + C2, +4.8%), respectively. The difference is intensified if there is a further increase to 3C with a reference capacity of  $86.0 \pm 3.1 \text{ mAh g}^{-1}$  (A + A, reference) to  $90.1 \pm 2.3 \text{ mAh g}^{-1}$  (B1 + B2, +4.7%) and  $95.5 \pm 1.6 \text{ mAh g}^{-1}$  (C1 + C2, +11.0%). For small C rates up to 1C, no difference between the layer configurations is observed. In contrast, at higher C rates, an improvement for a higher binder grading of the coating can be seen. This can be explained by the binder gradient introduced by the multilayer coatings. Due to the lower binder content at the separator, both

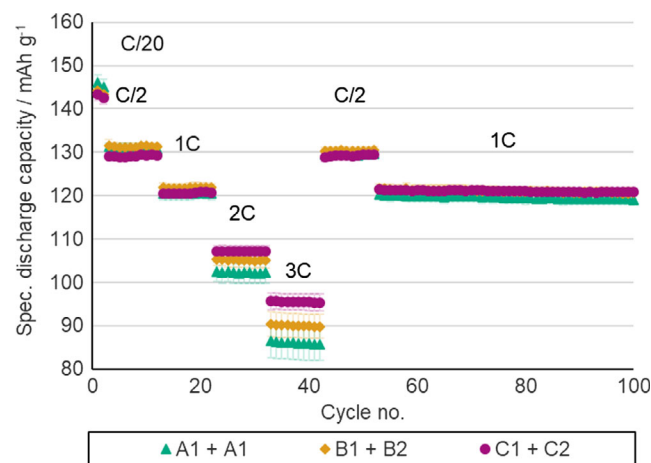


**Figure 10.** Specific discharge capacity of full cells for layer configuration A + A, B1 + B2, and C1 + C2 for normal capacity of  $2.05 \pm 0.08 \text{ mAh cm}^{-2}$ .

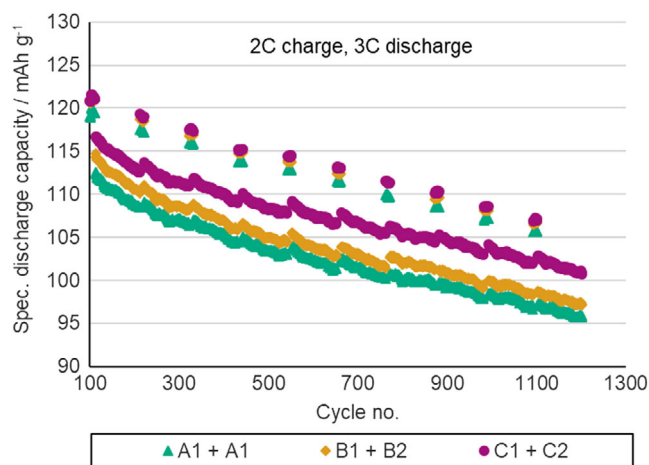


**Figure 11.** Long-term stability of multilayer electrodes. The cells were charged with 2C and discharged with 3C from cycle 100 to cycle 1200. Every 100 cycles, there are some 1C/1C steps for reference. The sample C1 + C2 with the highest binder gradient during coating shows the highest discharge capacity.

the diffusion pores are more open, and less binder is present on the surface of the graphite particles to limit interdiffusion. Due to the limitations of production under laboratory conditions, the layers with the same area capacity differ slightly, as shown in Table 2. Starting from A + A, B1 + B2 has a slightly less area weight and C1 + C2 has more area weight. The measured discharge capacities, in contrast, show a clear trend toward higher capacities with higher binder gradients after coating. The variation of the area loadings does not seem to have a significant influence with regard to the lower cathode capacity of 1.6 mAh cm<sup>-2</sup>.

After the C rate test, the electrodes were subjected to a cycle test (Figure 11) from cycle 100 to 1200. Here, the cells were charged with 2C and discharged with 3C, which represents a heavier load. For every 100 cycles some cycles were cyclized with 1C/1C for reference.

The long-term behavior also shows that the graded C1 + C2 configuration has the highest usable capacity at high C rates. The remaining capacity for A + A is 87.7%, for B1 + B2 87.6%, and for C1 + C2 89.1%. The higher adhesive force of the multilayered electrodes could contribute to the slightly better long-term stability of the cells.

It can be concluded that simultaneously coated two-layer electrodes show a higher specific discharge capacity up to 11.0%, especially at higher C rates of 2C and 3C, compared with the reference electrode configuration, and also show slightly better results in long-term behavior.

### 3. Conclusions

In this work, simultaneous two-layer slot die coating of LIB anodes was investigated. The coating stability was observed using a UV tracer in one layer and coating on a transparent PET substrate to visualize layer defects. It is shown that stable defect-free simultaneous two-layer coatings without intermixing can be produced

at coating speeds of 1–20 m min<sup>-1</sup>, which represents the maximum speed of the equipment used. Air entrainment emerges as the dominant failure criterion at lower wet film thickness and higher dimensionless gaps. In the layer configurations produced, both adhesive force and specific discharge capacity show better performance for two-layer configurations. The best performance is measured for a configuration with maximum SBR content at the current collector and no SBR content near the separator after the coating step, which leads to an improvement in discharge capacity up to 11% at 3C.

The binder migration during drying, however, ensures a certain distribution of the SBR binder.

Future work will investigate the relationship between two-layer coating with a binder gradient and different drying speeds, to reveal binder migration effects for high-capacity multilayer electrodes. Furthermore, the lower layer in this work has a relatively high binder content to generate a very high adhesive force. The layer thickness of this layer could be reduced in later work to minimize the overall amount of the binder content.

### 4. Experimental Section

**Slurry Materials and Preparation:** The major ingredient in the formulation was a slightly flaked graphite (SMG-A, Hitachi) as active material with an average particle size of 19 μm (D<sub>50</sub>). The conductive additive was carbon black (C65, Imerys). The binder system consisted of the two binders CMC (CMC Sunrose, Nippon Paper Industries) and SBR (BM-400, Zeon Corporation).

The anode slurry was prepared by dry mixing of the solids graphite and carbon black. The binder and dispersing agent CMC was dissolved in water and gradually added to the solids in three steps. A kneading device was used for the mixing steps with dispersing times of 10, 30, and 120 min after each dilution step. The solid content was set to 43 wt% after dilution. Subsequently, SBR dispersion was added in different amounts using a dissolver for 10 min. The viscosity was measured by a rotational viscometer in the plate-plate setup with 25 mm diameter (Anton Paar, Germany) from 0.01 to 10 000 s<sup>-1</sup>. The return path of the hysteresis measurement was evaluated to obtain constant shear history.

**Process Window Characterization:** A custom-made two-layer slot die was used. The distance between the slot die plates was adjusted with a polymer shim. Both slot exits to the coating bead were at the same height with a constant gap of 127 and 420 μm, respectively. Each slot was fed by a separate syringe pump with a predefined volume flow. For the investigation of the process window, a roll-to-roll pilot plant (Coatema BC43) was augmented with a custom characterization setup shown in Figure 12. The slot die was mounted in a 12 o'clock position against a glass plate. For visualization, a transparent PET substrate with a thickness of 50 μm was used to observe the moving contact lines in the coating bead by fixing a complementary metal–oxide–semiconductor (CMOS) sensor with macro-objective (Nikon D5600) below the glass plate. A second CMOS sensor was attached after the coating to monitor the top of the film. For investigation of layer intermixing, one layer was marked with UV fluorescent dye disodium 4,4'-bis(2-sulfonatostyryl)biphenyl (DSBB, TCI Chemicals). The fluorescent dye was brightened by a UV lamp. Starting with coating defects at low thickness, the wet film thickness was gradually increased until a stable coating was observed to examine the lower stability limit. The wet film thickness was further increased until swelling occurred at the upper stability limit. The coating speed was varied from 0.5 to 20 m min<sup>-1</sup>, which represented the maximum speed of the equipment used.

**Anode Coating, Drying, and Calendering:** The coating of the battery electrodes for further investigation was conducted with the same slot die on a batch coater. The current collector foil (copper foil, 10 μm Thickness, Nippon Mfg.) was applied to a temperature-controlled plate.

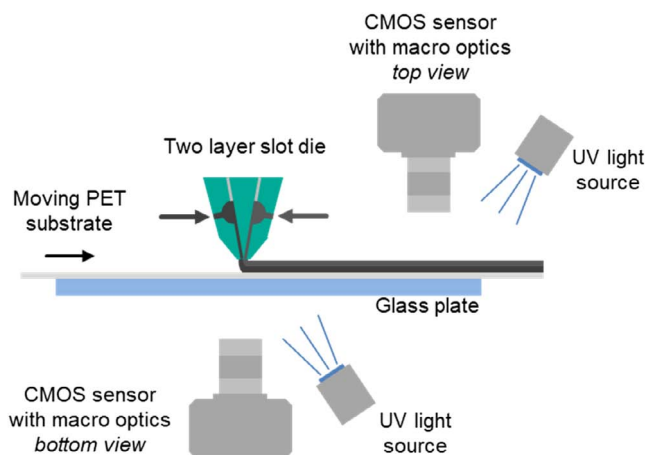


**Figure 12.** Coating setup for the investigation of coating stability and for characterization of the coating window with a two-layer slot die and two CMOS sensors and UV light sources for film inspection.

Subsequent to coating, the wet film was moved instantly below an impingement dryer with 20 slot nozzles in a row. To obtain homogeneous drying conditions, the plate was moved periodically back and forth until the electrode was dry. The drying rate was set to  $1.5 \text{ g m}^{-2} \text{ s}^{-1}$  at of  $38 \text{ }^\circ\text{C}$ . The dew point of the inlet air was  $3.1 \text{ }^\circ\text{C}$ . The average heat flux coefficient in the dryer was set to a constant value of around  $35 \text{ W m}^{-2} \text{ K}^{-1}$ . The dried electrode-layers were finally calendered to a porosity of 45% with heated rolls at  $50 \text{ }^\circ\text{C}$  (Saueressig GKL 200).

**Methods for Layer Characterization:** For adhesion characterization, a  $90^\circ$  peel test was used (AMETEK LS1 with 10 N load cell) as in previous works.<sup>[17]</sup> The electrode was cut into 30 mm strips with  $>40$  mm length and applied with the coating side to an adhesive stripe. The current collector foil was then pulled off at a maintained angle of  $90^\circ$  with a constant velocity of  $50 \text{ mm min}^{-1}$ . The required pull-off force was measured and divided by the sample width to obtain the adhesive line force.

**Cell Preparation and Test:** The electrodes were built into full cells in a pouch format ( $\approx 50 \text{ mm} \times 50 \text{ mm}$ , three full cells each electrode) and electrochemically examined. NMC 111 was used as active material for the cathode, (areal mass loading  $10.5 \text{ mg cm}^{-2}$ , capacity  $1.6 \text{ mAh cm}^{-2}$ ). A ceramic-coated nonwoven separator (SEPARION S240P30) was used. The electrolyte was a mixture of EC:EMC 1:1 with 1M  $\text{LiPF}_4$  (BASF LP30).

The rate capability was tested in CC mode with identical charging and discharging rates. After two formation cycles with C/20 the C-rate was varied between C/2 and 3C.

To investigate the long-term stability, cells were charged with 2C, followed by a constant voltage step at 4.2 V, until the current dropped to a value corresponding to C/20, followed by discharging with 3C. After 100 cycles, 10 cycles with 1C charging and 1C discharging were conducted. This procedure was repeated until 1200 cycles in total were achieved.

## Supporting Information

Supporting Information is available from the Wiley Online Library or from the author.

## Acknowledgements

The authors acknowledge financial support of Federal Ministry of Education and Research (BMBF) within the cluster project "ProZell High Energy" under the reference number 03XP0073B.

## Conflict of Interest

The authors declare no conflict of interest.

## Keywords

Li-ion anodes, process windows, simultaneous multilayer coatings, slot die coatings

Received: October 23, 2019

Revised: February 14, 2020

Published online: March 18, 2020

- [1] M. Yoshio, R. Brodd, A. Kozawa, *Lithium-Ion Batteries*, Springer, New York, NY **2009**.
- [2] B. Nykvist, M. Nilsson, *Nat. Clim. Chang.* **2015**, *5*, 329.
- [3] A. Thielmann, C. Neff, T. Hettesheimer, H. Döscher, M. Wietschel, J. Tübke, *Energiespeicher-Roadmap (Update 2017): Hochenergie-Batterien 2030+ und Perspektiven zukünftiger Batterietechnologien*, Fraunhofer-Institut für System-und Innovationsforschung ISI, Karlsruhe **2017**.
- [4] M. Singh, J. Kaiser, H. Hahn, *J. Electroanal. Chem.* **2016**, *782*, 245.
- [5] M. Müller, L. Pfaffmann, S. Jaiser, M. Baunach, V. Trouillet, F. Scheiba, P. Scharfer, W. Schabel, W. Bauer, *J. Power Sources* **2017**, *340*, 1.
- [6] S. Jaiser, A. Friske, M. Baunach, P. Scharfer, W. Schabel, *Dry. Technol.* **2017**, *35*, 1266.
- [7] S. Jaiser, M. Müller, M. Baunach, W. Bauer, P. Scharfer, W. Schabel, *J. Power Sources* **2016**, *318*, 210.
- [8] L. Pfaffmann, S. Jaiser, M. Müller, P. Scharfer, W. Schabel, W. Bauer, F. Scheiba, H. Ehrenberg, *J. Power Sources* **2017**, *363*, 460.
- [9] M. Baunach, S. Jaiser, S. Schmelzle, H. Nirschl, P. Scharfer, W. Schabel, *Dry. Technol.* **2016**, *34*, 462.
- [10] C. C. Li, Y. W. Wang, *J. Electrochem. Soc.* **2011**, *158*, 1361.
- [11] S. Lim, K. H. Ahn, M. Yamamura, *Langmuir* **2013**, *29*, 8233.
- [12] J. Nam, M. S. Carvalho, *J. Fluid Mech.* **2009**, *631*, 397.
- [13] H. S. Ji, W. G. Ahn, I. Kwon, J. Nam, H. W. Jung, *Chem. Eng. Sci.* **2016**, *143*, 122.
- [14] D. Liu, L. C. Chen, T. J. Liu, W. B. Chu, C. Tiu, *Energy Technol.* **2017**, *5*, 1235.
- [15] L. C. Chen, D. Liu, T. J. Liu, C. Tiu, C. R. Yang, W. B. Chu, C. C. Wan, *J. Energy Storage* **2016**, *5*, 156.
- [16] M. Schmitt, S. Raupp, D. Wagner, P. Scharfer, W. Schabel, *J. Coat. Technol. Res.* **2015**, *12*, 877.
- [17] J. Kumberg, M. Müller, R. Diehm, S. Spiegel, C. Wachsmann, W. Bauer, P. Scharfer, W. Schabel, *Energy Technol.* **2019**, *1900126*, 1.